Chapter 2

Aqueous electrolyte mediated reversible K^+ ion insertion in graphite

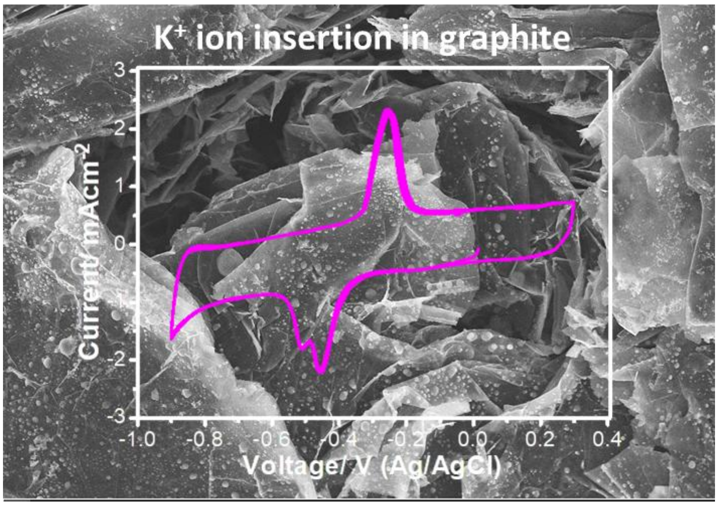

In this chapter, reversible K^+ ion insertion into graphite in an aqueous electrolyte is illustrated for the first time. It is shown that more facile diffusion of K^+ ions is possible in natural graphite than in pyrolytic graphite.

Ref.: R. Baishya, D. Sarmah, D. Mahanta, and S. K. Das, "Aqueous electrolyte-mediated reversible K^+ ion insertion into graphite," Physical Chemistry Chemical Physics, vol. 25, no. 36, pp. 24 298–24 302, 2023

2. Aqueous electrolyte mediated reversible K^+ ion insertion in graphite

2.1 Introduction

As discussed in the introduction chapter, carbon-based materials are gaining widespread popularity since the inception of rechargeable batteries. Among them, graphite is a simple yet an exceptionally rewarding material in the area of rechargeable lithium-ion battery. The success story of lithium-ion battery is well-crafted with the discovery of Li^+ ion being able to electrochemically diffuse, at a relatively low potential, in the structure of graphite to form a stage-1 graphite intercalation compound (GIC) with a composition of LiC_6, which results in a gravimetric and volumetric storage capacity of 372 $mAhg^{-1}$ and 850 $mAhcm^{-3}$ respectively [1]. In recent times however, there is a demand for non-lithium based rechargeable batteries due to scarcity and high cost of materials resources acutely necessary for the manufacturing of lithium-ion batteries. In view of it, the feasibility of energy storage devices based on earth abundant resources such as sodium, potassium, magnesium, zinc, aluminum etc. are under intense global investigation [2-7]. Taking leverage of the several advantages such as low-cost, high abundance and low toxicity, graphite always remains an attractive material of choice for other non-lithium-based systems [8-13]. The electrochemical stability of graphite for Na^+ ion storage is extensively studied and it was found that the electrochemical intercalation of Na^+ ion in graphite is quite challenging and it could exhibit a specific capacity of only around 35 $mAhg^{-1}$ in traditional non-aqueous carbonate-based electrolyte with a scope for improvement up to about 110 $mAhg^{-1}$ with solvent co-intercalation method [8-10]. Recently, it was also revealed that large size anions such as $AlCl_4^-$ could be reversibly intercalated in graphite in chloroaluminate electrolyte for aluminum-ion battery [11, 12]. Similarly, there are ample examples of K^+ ion insertion and extraction in graphitic materials [14,15]. GIC with K^+ ion as guest was shown to be formed by vapor phase method, solution method and electrochemical method. For example, Mizutani et al. demonstrated the formation of stage-1 K-GIC (potassium graphite intercalation compound) by intercalation of K^+ ion in 2-methyltetrahydrofuran [14]. Utilizing molten KF electrolyte, Liu et al. illustrated the electrochemical intercalation of K^+ ion into graphite, but at a relatively high temperature (1163 K) [15]. Until recently, the electrochemical K^+ ion intercalation in graphite was unexplored at room temperature. Jian et al. first reported the formation of stage-1 K-GIC upon electrochemical K^+ ion insertion in graphite in non-aqueous carbonate electrolyte [16]. Liu et al. also verified the potassiation in disordered carbon with carbonate electrolyte [17]. However, to the best of our knowledge, electrochemical storage of K^+ ion in graphite from aqueous electrolytes is hitherto been unknown. The hydrated radius of K^+ ion (3.31 Å) is relatively smaller than Li^+ ion (3.82 Å) and Na^+ ion (3.58 Å) [18]. Therefore, the mobility of K^+ ion is relatively higher than the Li^+ and Na^+ ions in an electrolyte which is an important parameter for delivering high power by an electrochemical cell [19]. In the current chapter, reversible K^+ ion insertion in graphite in aqueous electrolyte is explored for the first time and the effect of types of graphite and electrolyte on the insertion process have been presented. Pyrolytic graphite and natural graphite were used for the study. For another set of experiments, exfoliated natural graphite was utilized. The exfoliation was performed using a full cell comprising of graphite as positive electrode and Cu foil as negative electrode in an aqueous electrolyte [20].

2.2 Experimental Section

2.2.1 Materials

Two types of graphite were used for the study. Pyrolytic graphite (0.017 mm) and natural graphite (0.5 mm) foils were obtained commercially. These foils were cleaned with ethanol prior to use and no other chemical treatment was performed unless specified. For another set of experiments, exfoliated natural graphite was utilized and the exfoliation was performed as reported by our group earlier and the surface of this exfoliated graphite consists of graphitic nanoflakes.

2.2.2 Characterization

Structural and morphological investigations were carried out using techniques such as XRD (BRUKER AXS D8 FOCUS; Cu-K_α radiation, $\lambda = 1.5406$ Å), Raman spectroscopy (RENISHAW BASIS SERIES having 514 laser excitation), atomic force microscopy and contact angle measurement. Raman experiments were performed in two types of natural graphite; one in pristine form another one with electrochemical experiments performed on it. The samples were washed and dried properly before performing Raman analysis. For ex-situ measurements, the graphite electrodes were cleaned with DI water after the electrochemical experiments and these electrodes were dried at 100°C for 12 h. The XPS measurements were performed in two sets of natural graphite electrodes. In the first set, electrochemical measurements were done in the graphite sheet and the XPS measurements were recorded. Whereas in the second set, the XPS measurements were recorded after dipping the natural graphite electrode in KOH (for 24 hour) and letting it to dry in ambient condition. In both the cases, electrodes were washed and dried properly before performing the XPS measurement. All experiments were carried out at room temperature and under ambient atmosphere.

2.2.3 Electrochemical analysis

Cyclic voltammetry (CV) and galvanostatic discharge/charge experiments were performed in a conventional three-electrode electrochemical glass cell with graphite foil, Pt electrode and an aqueous Ag/AgCl electrode (in KCl solution) as working, counter and reference electrodes respectively. The utilized electrolyte was an aqueous solution of KOH (purity of 84%) of varying concentrations. The discharge/charge and CV experiments were performed in the voltage range of -0.9 V to 0.3 V. Electrochemical impedance spectroscopy was performed in the frequency range of 1 mHz -200 kHz with a signal amplitude of 10 mV.

The Diffusion coefficient ($D_K{}^+$) can be estimated from the following Equation (Ref. 31,32):

$$D_K^+ = 0.5\left(\frac{RT}{An^2F^2C\sigma_w}\right)^2$$

where R is the gas constant (8.314 J mol^{-1} K^{-1}), T is the absolute temperature (298.15 K), A is the surface area of the electrode (1 cm^2), n is the number of electrons transferred, F is Faraday constant (96500 C mol^{-1}), C is the concentration of K^+ ion in the solution (6 M), and σ_w is the Warburg coefficient, which is calculated by the following Equation (at low-frequency region).

$$Z' = R_S + R_{CT} + \sigma_w \omega^{-0.5}$$

where R_S is the electrolyte resistance, R_{CT} is the charge transfer resistance, σ_w can be obtained from the slope of linear fitting of the real part of impedance (Z') vs. the reciprocal square root of angular frequency ($\omega^{-0.5}$).

2.3 Results and Discussion

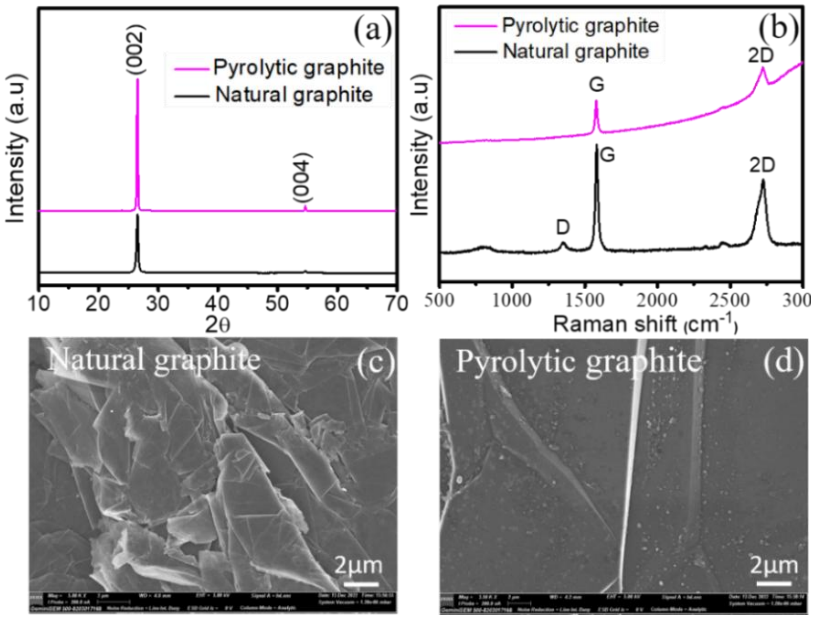

Figure 2.1 (a) XRD patterns, (b) Raman spectra and (c,d) FESEM images of Natural and Pyrolytic graphite.

Figure 2.1a shows the XRD patterns of the two types of graphite and it could be noted that both show the characteristics of graphitic carbon. The Raman spectra however show a distinction between them. The Raman spectrum of natural graphite shows the three characteristics G, D and 2D bands at 1351 cm^{-1}, 1575 cm^{-1} and 2373 cm^{-1} respectively. In contrast, only G and 2D bands are visible for pyrolytic graphite (Figure 2.1b). It is noted here that G, D and 2D bands represent the vibration mode of E_{2g} along the hexagonal carbon layer, some structural disorder and two-phonon second order band without any kind of disorder or defects respectively [21]. FESEM images show similar surface morphology for both types of graphite (Figure 2.1(c,d))

Figure 2.2a shows the CV profiles of natural graphite in 1 M KOH electrolyte at a scan rate of 2.5 mVs^{-1}. There is one broad pair of cathodic and anodic peaks at -0.5 V and -0.2 V respectively. Interestingly, when the concentration of the KOH electrolyte was changed to 6 M, it apparently appears that the cathodic peak is a superimposition of two peaks at -0.59 V and -0.53 V (Figure 2.2b). The cathodic and anodic peak separation is smaller for the 6 M KOH (260 mV) than 1 M KOH (350 mV). Experiments were also performed with exfoliated graphite and a similar trend was also observed for it (Figure 2.2c). However, the two cathodic peaks could now be prominently identified at -0.45 V and 0.51 V for the 6 M KOH electrolyte. The cathodic and anodic peak separation in this case is 200 mV. The pyrolytic graphite shows no electrochemical activity as could be seen from figure 2.2d.

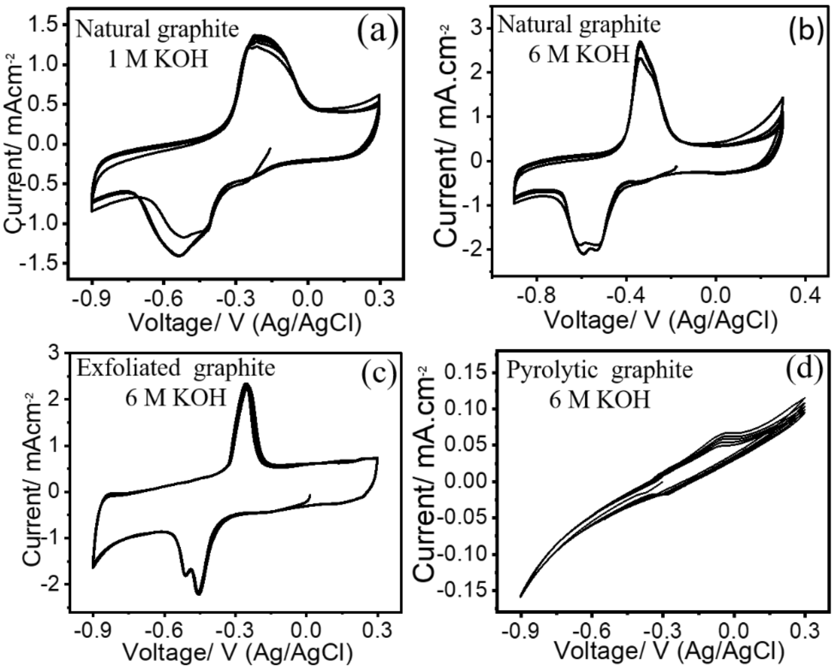

Figure 2.2 CV profiles of Natural graphite in aqueous (a) 1M KOH, (b) 6M KOH, CV profiles of (c) exfoliated graphite and (d) pyrolytic graphite in 6 M aqueous KOH at a scan rate of 2.5 mVs^{-1}

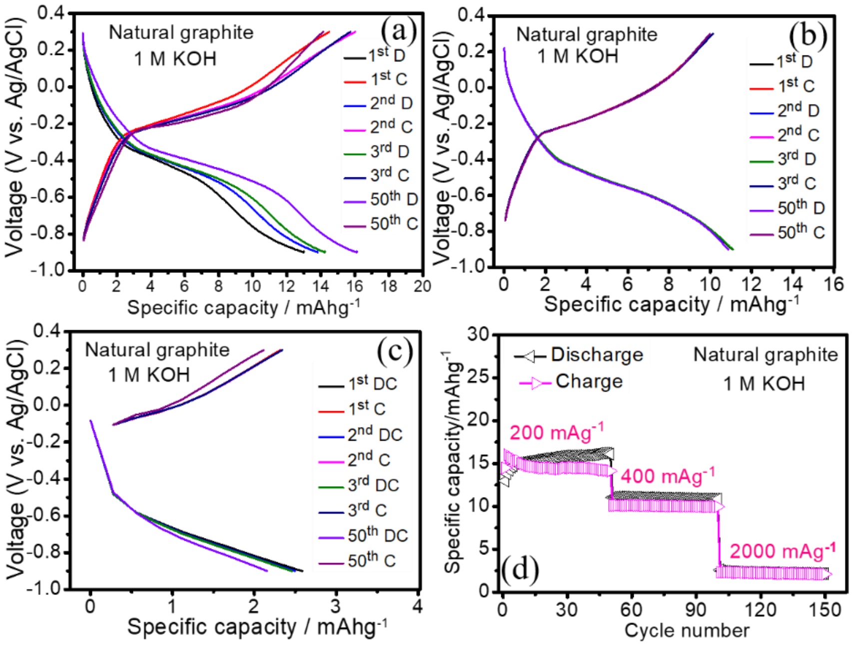

Figure 2.3 Galvanostatic discharge/charge profiles of (a) 200 mAg^{-1}, (b) 400 mAg^{-1}, (c) 2000 mAg^{-1} and (d) rate capability measurement of natural graphite in 1 M KOH aqueous electrolyte.

The consistency of the CV profiles was further corroborated with galvanostatic charge/discharge experiments. Figure 2.3 and 2.4 show the charge-discharge profiles of natural graphite in 1 M and 6 M KOH respectively at current rate of 200 mAg^{-1}. It could be seen that natural graphite shows a discharge plateau around - 0.33 to -0.52 V for 1 M KOH (Figure 2.3a). On the other hand, two discharge potential plateaus at -0.50 V and -0.57 V with a charge potential plateau at -0.4 V could be noticed when the electrolyte was 6 M KOH (Figure 2.4a). The specific capacities are almost similar for both 1 M and 6 M KOH electrolytes at 200 mAg^{-1}. However, noticeable difference could be seen at higher current rates (Figure 2.3 and 2.4). It is easily inferred that high current rates are sustained for the 6 M KOH electrolyte. The specific capacity is only 2.4 mAhg^{-1} for 1 M KOH electrolyte, where as it is 8 mAhg^{-1} for 6 M KOH electrolyte at the current rate of 2 Ag^{-1} (figure 2.3(b,c) and 2.4(b,c)). It is noted here that the ionic conductivity may play a vital role here since the conductivity of 6 M KOH (~ 6.26 x 10^{-4} Scm^{-1}) is higher than 1 M KOH (~ 2.15 x 10^{-4} Scm^{-1}) [22].

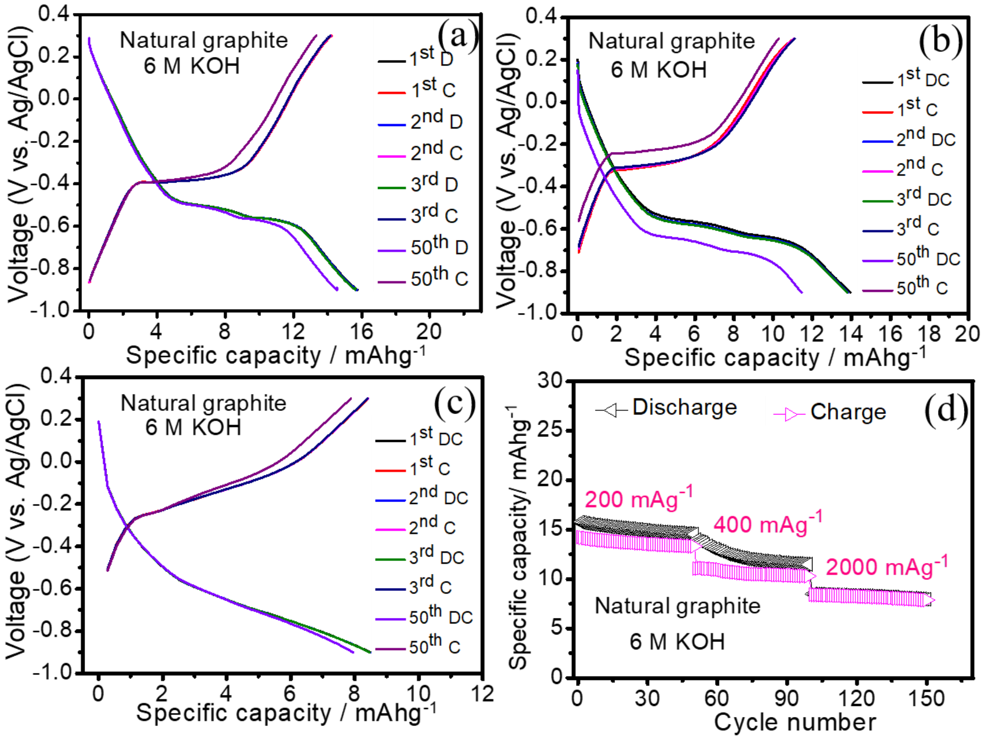

Figure 2.4 Galvanostatic discharge/charge profiles of (a) 200 mAg^{-1}, (b) 400 mAg^{-1}, (c) 2000 mAg^{-1} and (d) rate capability measurement of natural graphite in 6 M KOH aqueous electrolyte.

The charge-discharge profiles obtained with exfoliated graphite also indicate a similar pattern in 6 M KOH electrolyte (Figure 2.5). In this case also, two almost closely spaced discharge potential plateaus could be noticed whereas only one discharge potential is seen for 1 M KOH electrolyte (Figure 2.6a). The exfoliated natural graphite also shows higher specific capacities in comparison to pristine natural graphite (Figure 2.5, 2.6 and 2.7). It is also noted here that there is negligible decline in specific capacities over the measured number of charge-discharge cycles unlike severe capacity fading as was observed in case of non-aqueous electrolyte [16]. The overpotential is 130 mV in the case of exfoliated graphite in 6 M KOH, whereas it is 270 mV for pristine graphite in 6 M KOH (measured at 40% of initial discharge/charge capacity i.e., at the plateau region) (Figure 2.5a). Supporting the CV data, pyrolytic graphite fails to show any noticeable specific capacity even at a slow current rate of 200 mAg^{-1} (Figure 2.8).

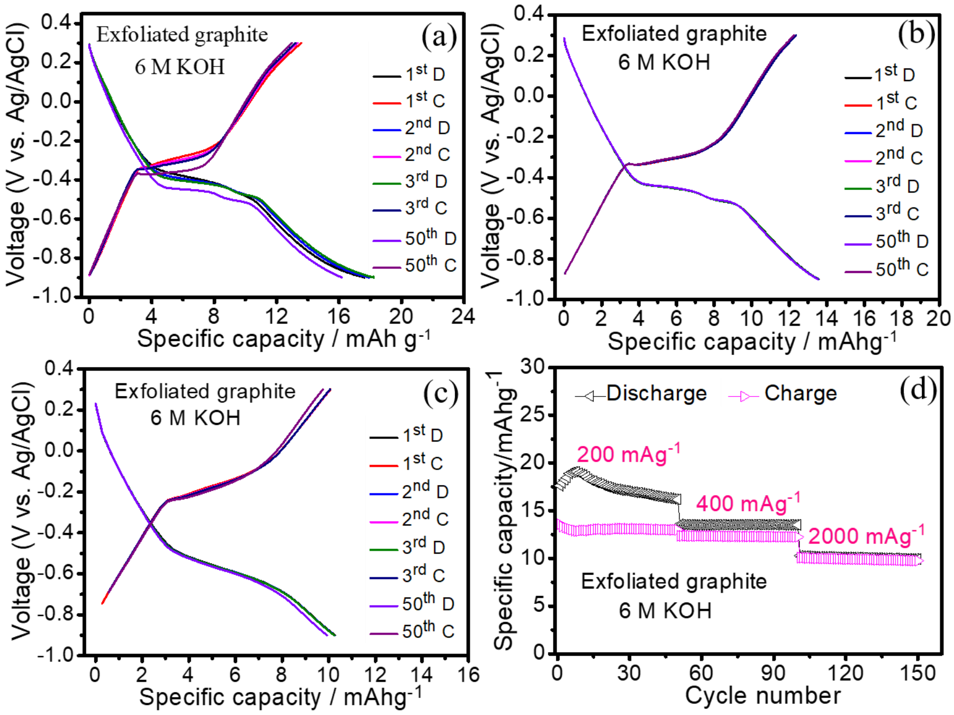

Figure 2.5 Galvanostatic discharge/charge profiles of (a) 200 mAg^{-1}, (b) 400 mAg^{-1}, (c) 2000 mAg^{-1} and (d) rate capability measurement of exfoliated graphite in 6 M KOH aqueous electrolyte.

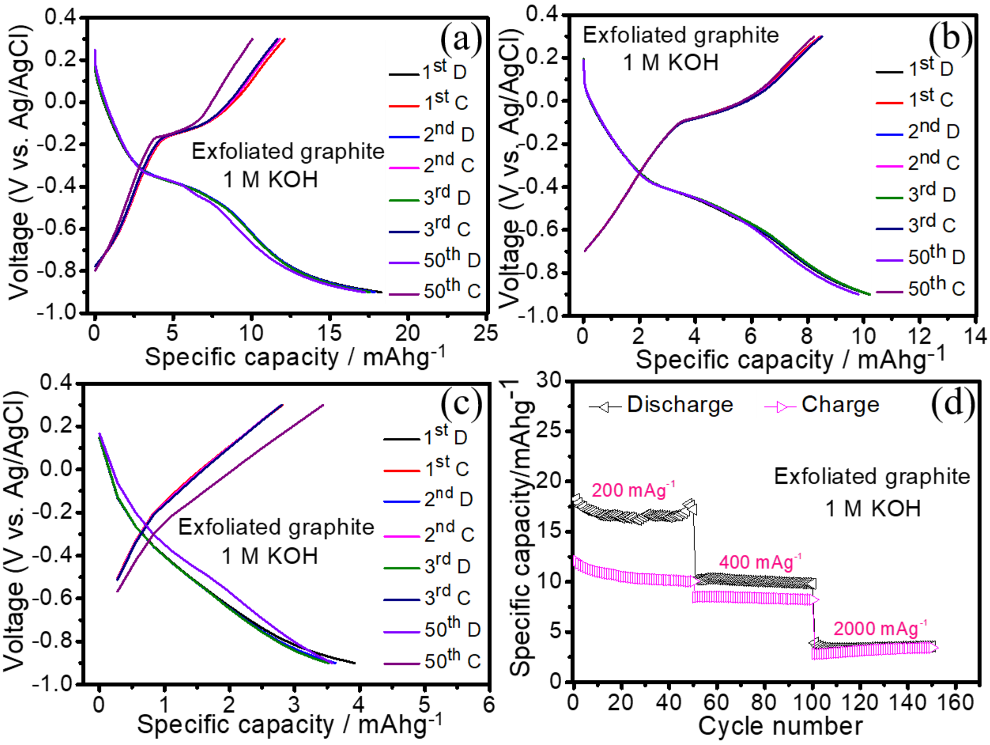

Figure 2.6 Galvanostatic discharge/charge profiles of (a) 200 mAg^{-1}, (b) 400 mAg^{-1}, (c) 2000 mAg^{-1} and (d) rate capability measurement of exfoliated graphite in 1 M KOH aqueous electrolyte.

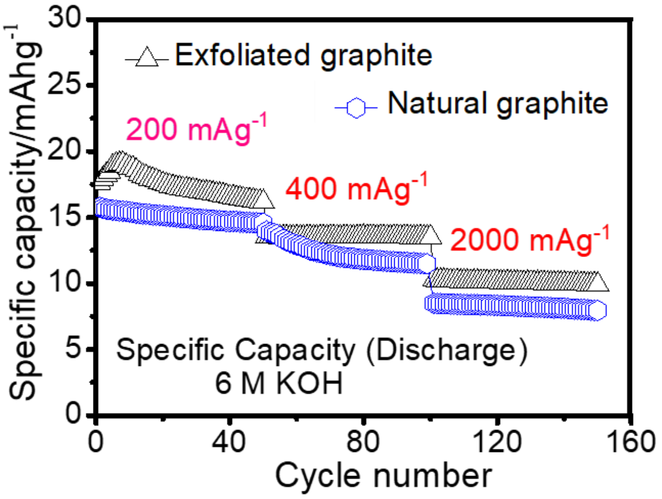

Figure 2.7 Comparison of Rate capability measurement of normal and exfoliated graphite in 6 M KOH aqueous electrolyte.

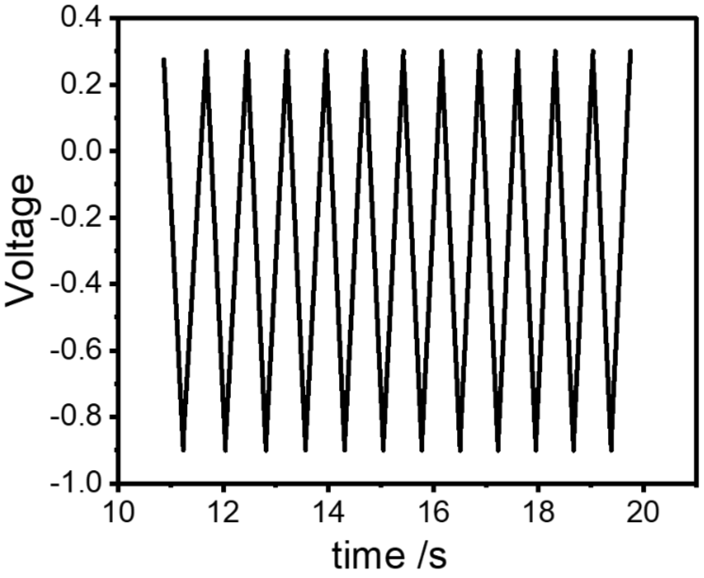

Figure 2.8 Charge/discharge curve of pyrolytic graphite in 6 M KOH electrolyte at 200 mAg^{-1}.

In order to understand the electrochemical mechanism, CV experiments were performed at different scan rates for natural graphite in 6 M KOH electrolyte and CV profiles are shown in Figure 2.9a. The cathodic and anodic peak current responses were plotted against the square root of the scan rates (Figure 2.9b) and it was found to be linearly proportional suggesting a possible diffusion-controlled process as per Randles-Sevcik relationship [23]. To make a quantitative estimation of the diffusion process, CV profiles were analyzed using the following relationships: (i) $\mathrm{i(V)} = \mathrm{K}_1\vartheta + \mathrm{K}_2\vartheta^{\frac{1}{2}}$(ii) $\frac{\mathrm{i(V)}}{\vartheta^{\frac{1}{2}}} = \mathrm{K}_1\vartheta^{\frac{1}{2}} + \mathrm{K}_2$. Here, the term $\mathrm{K}_1\vartheta$ gives the capacitive part and $\mathrm{K}_2\vartheta^{\frac{1}{2}}$ gives the diffusive contribution to the overall ion storage process [23]. It is again found that diffusion-controlled storage process is quite dominant over the capacitive storage process and the diffusive contribution is higher than 80 % (Figure 2.9 (c-e)). This analysis gives an indication that the observed electrochemical activity is mainly due to K^+ ion insertion and extraction in natural graphite.

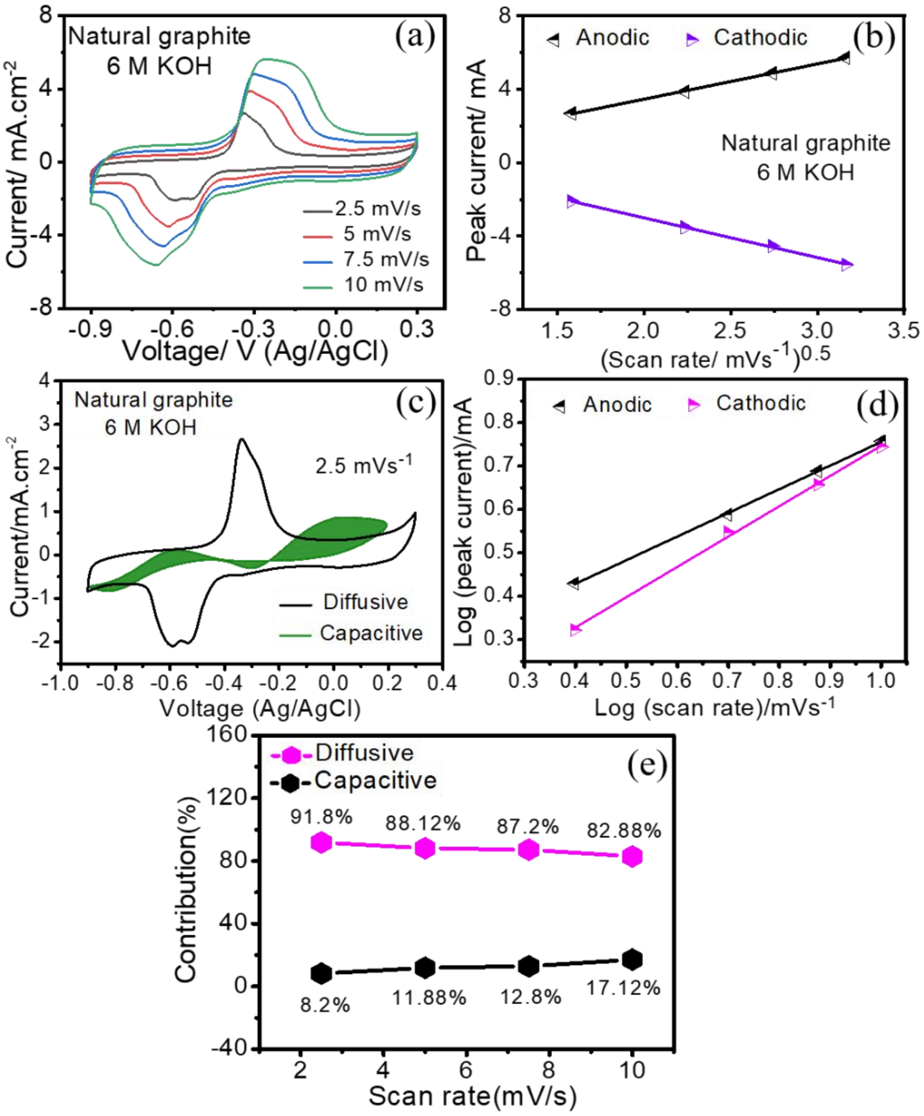

Figure 2.9 (a) CV curves of natural graphite at different scan rates and (b) plot of peak current vs scan rate. (c) Capacitive and diffusive contributions for 6 M KOH in natural graphite at 2.5 mVs^{-1}, (d) Log (peak current) vs Log (scan rate), (e) Diffusive and capacitive contributions in percentage. The electrolyte is 6 M aqueous KOH.

To further identify any change in the structure of the natural graphite electrode during potassiation and depotassiation, the electrodes were removed after specific number of charge/discharge cycles and interrogated with ex-situ XRD measurements. Although there is no major change in the XRD pattern after the 1st discharge cycle, the peak at 2θ = 26.53° shifts to lower angle after subsequent discharge cycles with a noticeable shift of 0.37° for the 50th discharged cycle electrode as shown in figure 2.10 (a,b). The ex-situ Raman spectrum of the discharged state natural graphite electrode also shows a lower shift, in the G band by an amount of 5.5 cm^{-1} (Figure 2.10 (c,d)). Similar effect was also observed for K$^+$ ion insertion in graphite in non-aqueous electrolyte [24]. The most striking feature is the change in the intensity of the disorder peak (D band). The intensity ratio of D to G band i.e., I_D/I_G is 0.11 and 0.17 for the pristine and discharged state graphite electrodes respectively, which indicates a 55 % rise in disorder in the graphite electrode after potassiation (Figure 2.10 c). Ex-situ XPS measurement also confirms the presence of K species in the discharged state natural graphite electrode. Figure 2.11 shows the characteristic K2p$_{3/2}$ and K2p$_{1/2}$ at 290.46 eV and 293.50 eV respectively. In order to confirm that this K signal is not due to mere adsorption of K$^+$ ions, an additional XPS measurement on a graphite electrode submerged in 6 M KOH for 24 h was performed. The corresponding XPS spectrum is shown in Figure 2.12. It could be seen that there is no noticeable K-signal (Figure 2.12 b). AFM images, as shown in figure 2.13 (a-d), also show change in the surface texture of the graphite electrode. The swelling of the surface could be clearly noticed after potassiation from the 3D height map. There is significant difference in the height profile of the discharged state and pristine graphite electrodes. This is also supported by the FESEM images obtained after discharge (Figure 2.13 (e,f)).

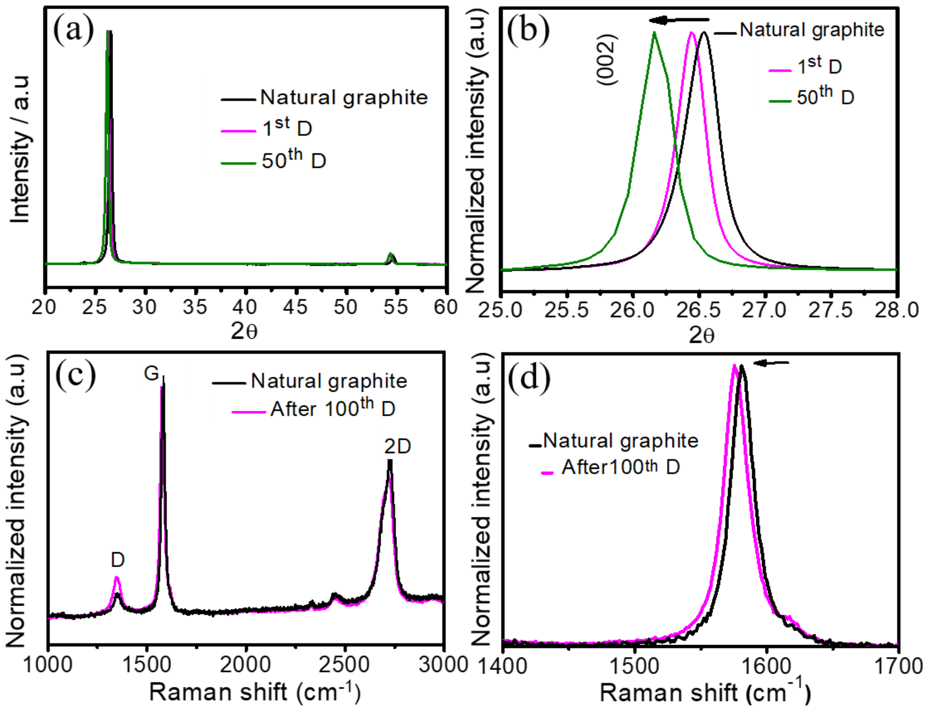

Figure 2.10 (a-b) Ex-situ XRD analysis, (c-d) Raman spectra of pristine graphite, natural graphite after 1st and 50th Discharge.

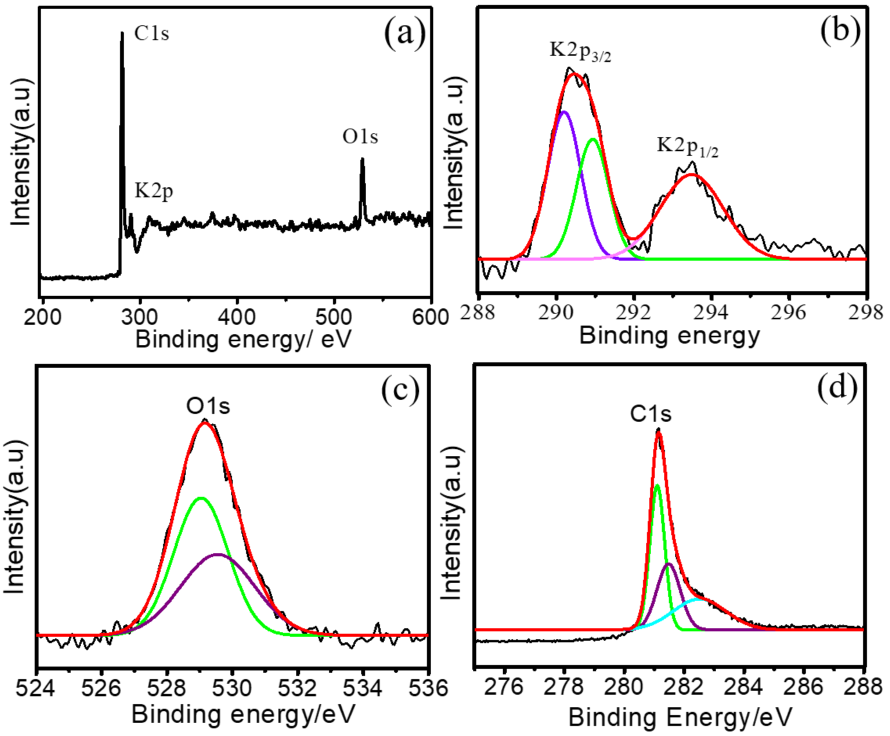

Figure 2.11 High resolution XPS spectra for (a) Full XPS spectrum, (b) C 1s, (c) O 1s peaks and (d) O1s.

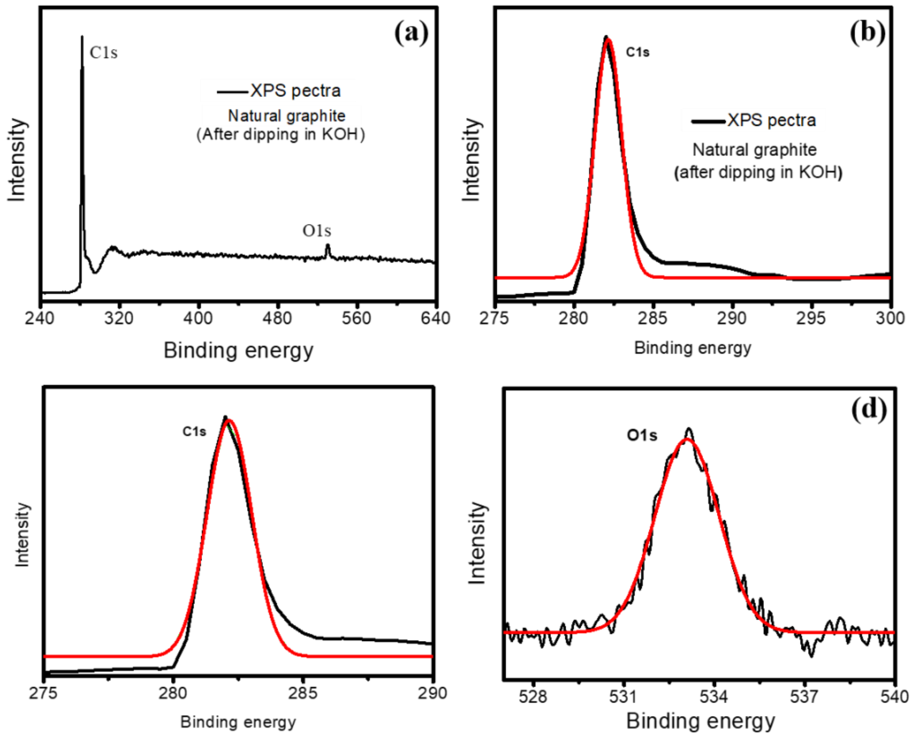

Figure 2.12 High resolution XPS spectra (after dipping natural graphite in KOH) for (a) full XPS spectra, (b) C 1s peak (no K2p peaks), (c) enlarged C 1s and (d) O 1s.

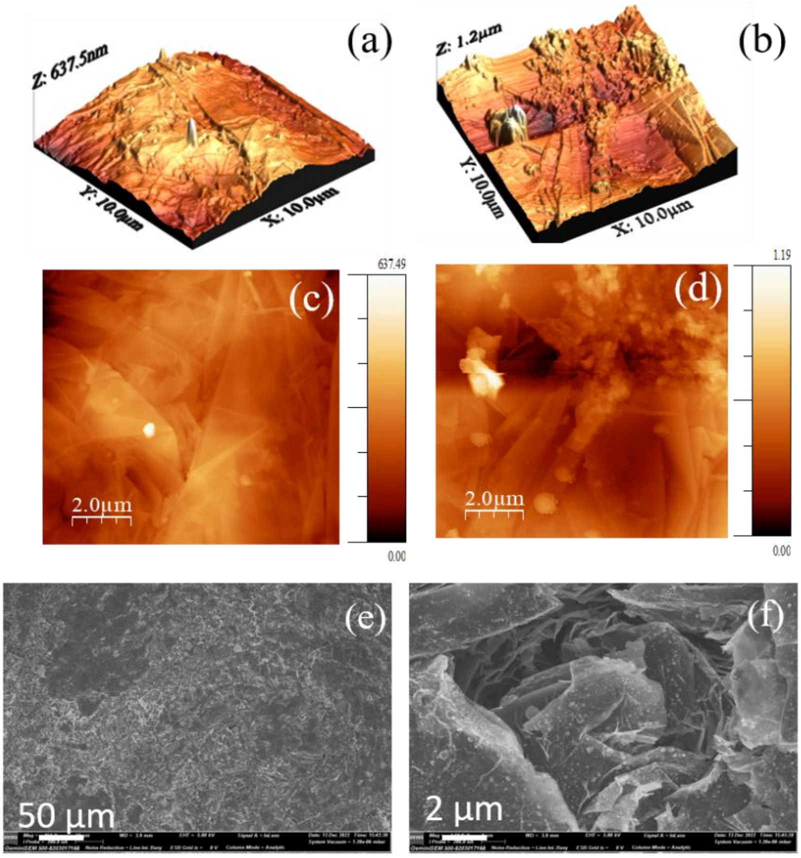

Figure 2.13 AFM images of natural graphite (a,c) before discharge, (b,d) after discharge and (e,f) FESEM image of natural graphite after discharge.

Contact angle measurement was also performed to see any changes in the wettability of the natural graphite electrode. It is seen that the natural graphite electrode after discharge shows a smaller contact angle (54.6°) than the pristine natural graphite electrode (68.7°) (figure 2.14 (a,b)). In order to find that the mere dipping of the electrode in the electrolyte while discharging did not change the contact angle, the same was measured for a natural graphite electrode dipped in 6 M KOH electrolyte for 12 h. It is seen that the contact angle in this case (68.5°) is similar to the contact angle for pristine natural graphite electrode (figure 2.14c). It signifies that electrochemical K^+ ion insertion changes the wettability of the electrode. This intriguing process of change of contact angle under a bias potential in an electrolytic medium is known as 'Electrowetting" [25]. Several interesting recent studies on graphite/graphene electrode indicate decrease in the contact angle upon cation or anion insertion in both aqueous and non-aqueous electrolytes akin to our observations [25-30]. EIS measurements (figure 2.14d) also show that the charge transfer resistance for the natural graphite electrode is much lower in comparison to the pyrolytic graphite electrode. The K^+ ion diffusion coefficient was estimated from the EIS data following a well-known procedure as described earlier and the diffusion co-efficient is found to be of the order of 10^{-19} cm^2s^{-1} (figure 2.14e) [31,32]. It is to be noted that this value is much lower in comparison to Li^+ ion (~ 10^{-11} cm^2s^{-1}) and K^+ ion (~10^{-9} cm^2s^{-1}) diffusion co-efficient in graphite in non-aqueous electrolyte [33,34]. The slow diffusion may be a reason for low specific capacity. It could be a possibility to enhance the performance by the utilization of few layers graphitic foam or highly crystalline graphitic foam as demonstrated earlier for Al-battery research [35,36]. It is important to discuss here the electrochemical processes that may possibly occur. The ex-situ XRD and ex-situ Raman measurements unable to give a clear verdict on the possible formation of K-GIC as was evidenced for non-aqueous systems [37,39]. Therefore, a plausible explanation is given exclusively based on the electrochemical outcomes [40,41]. A careful inspection of the CV profiles (for example Figure 2.2c) indicates both surface mediated and insertion process. Following the standard protocol of distinguishing surface and intercalation storage, it could be seen that if there were no redox activities in the potential region of -0.6 V to -0.2 V, the CV profiles resemble a rectangular feature which is indicative of capacitive charge storage (or adsorption of charged species) [41]. On the other hand, the appearance of the sharp cathodic and anodic peaks (Figure 2.2c) is indication of intercalation based redox activities. The charge/discharge profiles (for example Figure 3c) also underpin this phenomenon. There is presence of long discharge potential plateaus which is a trait of insertion-based electrodes. Such potential plateaus are typical of $LiFePO_4$ or $LiMn_2O_4$ type of cathode materials for Li-ion batteries where Li^+ ion intercalation/deintercalation is the only dominating process [42-46]. Again, the charge/discharge profiles also show linear behaviors in the potential range of 0.3 V to -0.3 V and -0.5 V to -0.9 V (Figure 2.4a). Generally, the linear potential response corresponds to surface storage [41]. As already discussed, using figure 2.9 (c-e), there is capacitive contribution in the present case. Therefore, it could be commented that there is signature of both the insertion and adsorption processes [47].

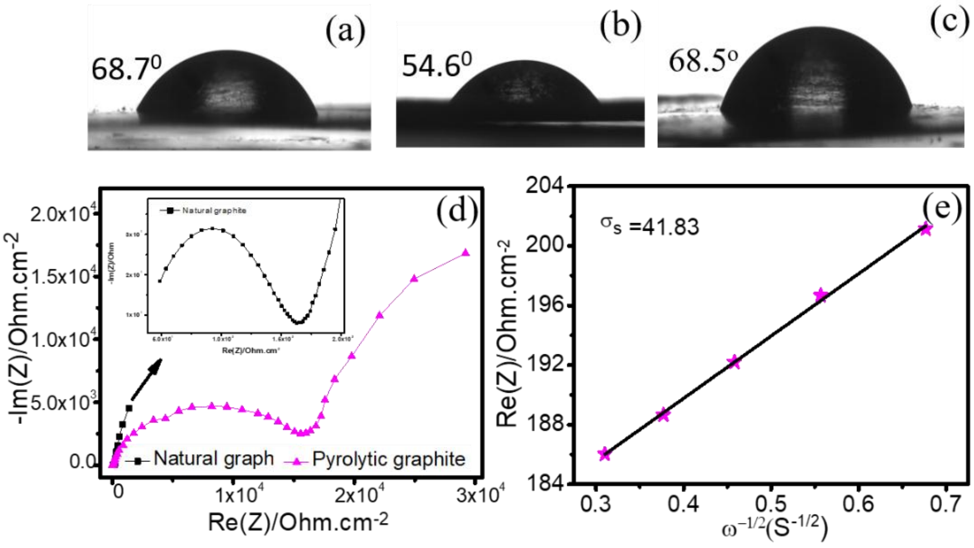

Figure 2.14 (a-c) Contact angle measurement for natural graphite, EIS spectra for (d) natural graphite and pyrolytic graphite, (e) The relationship curve between Z′ and $\omega^{-1/2}$ in the low-frequency range for natural graphite in 6 M KOH.

2.3 Conclusion

In summary, this chapter explains the reversible K^+ ion insertion in natural graphite in aqueous electrolyte in this chapter. It is found that not only the type of graphite but also the concentration of the electrolyte plays an important role in the storage process. It is revealed that pyrolytic graphite fails to host K^+ ion. It is also obtained that the K^+ ion insertion significantly enhanced the wettability of the graphite electrode which promotes ion insertion kinetics. A careful observation from Raman spectra of discharged state natural graphite electrode depicts 55% rise in disorder followed by potassiation. Exfoliated graphite shows reduced overpotential in comparison to natural graphite in 6 M aqueous KOH electrolyte. Additionally, various ex-situ characterization techniques confirm potassium ion insertion in the natural graphite electrode during cycling. It is also found that diffusion-controlled storage process is quite dominant over the capacitive storage process.

2.4 References

[1] Asenbauer, J., Eisenmann, T., Kuenzel, M., Kazzazi, A., Chen, Z. and Bresser, D. The success story of graphite as a lithium-ion anode material–fundamentals, remaining challenges, and recent developments including silicon (oxide) composites. *Sustainable Energy Fuels*, 4(11): 5387-5416, 2020.

[2] Canepa, P., Sai Gautam, G., Hannah, D.C., Malik, R., Liu, M., Gallagher, K.G., Persson, K.A. and Ceder, G. Odyssey of multivalent cathode materials: open questions and future challenges. *Chemical Reviews*, 117(5): 4287-4341, 2017.

[3] Liang, Y., Dong, H., Aurbach, D. and Yao, Y. Current status and future directions of multivalent metal-ion batteries. *Nature Energy*, 5(9): 646-656, 2020.

[4] Schroeder, M.A., Ma, L., Pastel, G. and Xu, K. The mystery and promise of multivalent metal-ion batteries. *Current Opinion in Electrochemistry.* 29: 100819, 2021.

[5] Anoopkumar, V., John, B. and Mercy, T.D. Potassium-ion batteries: key to future large-scale energy storage? *ACS Applied Energy Materials*, 3(10): 9478-9492, 2020.

[6] Min, X., Xiao, J., Fang, M., Wang, W.A., Zhao, Y., Liu, Y., Abdelkader, A.M., Xi, K., Kumar, R.V. and Huang, Z. Potassium-ion batteries: outlook on present and future technologies. *Energy Environmental Science*, 14(4): 2186-2243,2021.

[7] Elia, G.A., Kravchyk, K.V., Kovalenko, M.V., Chacón, J., Holland, A. and Wills, R.G.An overview and prospective on Al and Al-ion battery technologies. *Journal of Power Sources*, 481: 228870, 2021.

[8] Wen, Y., He, K., Zhu, Y., Han, F., Xu, Y., Matsuda, I., Ishii, Y., Cumings, J. and Wang, C. Expanded graphite as superior anode for sodium-ion batteries. *Nature Communication*, 5(1): 4033, 2014.

[9] Stevens, D.A. and Dahn, J.R., 2001. The mechanisms of lithium and sodium insertion in carbon materials. *Journal of Electrochemical Society*, 148(8): A803, 2001.

[10] Jache, B. and Adelhelm, P. Use of graphite as a highly reversible electrode with superior cycle life for sodium-ion batteries by making use of co-intercalation phenomena. *Angewandte Chemie International Edition*, 53(38): 10169-10173, 2014.

[11] Angell, M., Pan, C.J., Rong, Y., Yuan, C., Lin, M.C., Hwang, B.J. and Dai, H., 2017. High Coulombic efficiency aluminum-ion battery using an AlCl3-urea ionic liquid analog electrolyte. *Proceedings of the National Academy of Sciences*, 114(5): 834-839, 2017.

[12] Elia, G.A., Greco, G., Kamm, P.H., García-Moreno, F., Raoux, S. and Hahn, R. Simultaneous X-Ray Diffraction and Tomography Operando Investigation of Aluminum/Graphite Batteries. *Advanced Functional Materials*, 30 (43): 2003913, 2020.

[13] Li, Y., Lu, Y., Adelhelm, P., Titirici, M.M. and Hu, Y.S. Intercalation chemistry of graphite: alkali metal ions and beyond. *Chemical Society Reviews*, 48(17): 4655-4687, 2019.

[14] Mizutani, Y., Abe, T., Ikeda, K., Ihara, E., Asano, M., Harada, T., Inaba, M. and Ogumi, Z. Graphite intercalation compounds prepared in solutions of alkalimetals in 2-methyltetrahydrofuran and 2, 5-dimethyltetrahydrofuran. *Carbon*, 35(1): 61-65, 1997.

[15] Liu, D., Yang, Z., Li, W., Qiu, S. and Luo, Y. Electrochemical intercalation of potassium into graphite in KF melt. *Electrochimica Acta*, 55(3): 1013-1018, 2010.

[16] Jian, Z., Luo, W. and Ji, X. Carbon electrodes for K-ion batteries. *Journal of American Chemical Society*, 137(36): 11566-11569, 2015.

[17] Liu, Y., Fan, F., Wang, J., Liu, Y., Chen, H., Jungjohann, K.L., Xu, Y., Zhu, Y., Bigio, D., Zhu, T. and Wang, C. In situ transmission electron microscopy study of electrochemical sodiation and potassiation of carbon nanofibers. *Nano Letters*, 14(6): 3445-3452, 2014.

[18] Chao, D., Zhou, W., Xie, F., Ye, C., Li, H., Jaroniec, M. and Qiao, S.Z. Roadmap for advanced aqueous batteries: From design of materials to applications. *Science Advances*, 6(21): 4098, 2020.

[19] Komaba, S., Hasegawa, T., Dahbi, M. and Kubota, K. Potassium intercalation into graphite to realize high-voltage/high-power potassium-ion batteries and potassium-ion capacitors. *Electrochemical Communications*, 60: 172-175, 2015.

[20] Nandi, S. and Das, S.K. Realizing a low-cost and sustainable rechargeable aqueous aluminum-metal battery with exfoliated graphite cathode. *ACS Sustainable Chemistry & Engineering*, 7(24): 19839-19847, 2019.

[21] Inagaki, M. and Kang, F. Graphene derivatives: graphane, fluorographene, graphene oxide, graphyne and graphdiyne. *Journal of Material Chemistry A*, 2(33): 13193-13206, 2014.

[22] Gilliam, R.J., Graydon, J.W., Kirk, D.W. and Thorpe, S.J. A review of specific conductivities of potassium hydroxide solutions for various concentrations and temperatures. *International Journal of Hydrogen Energy*, 32(3): 359-364, 2007.

[23] Brezesinski, T., Wang, J., Polleux, J., Dunn, B. and Tolbert, S.H. Templated nanocrystal-based porous TiO_2 films for next-generation electrochemical capacitors. *Journal of American Chemical Society*, 131(5): 1802-1809, 2009.

[24] Luo, W., Wan, J., Ozdemir, B., Bao, W., Chen, Y., Dai, J., Lin, H., Xu, Y., Gu, F., Barone, V. and Hu, L. Potassium ion batteries with graphitic materials. *Nano Letters*, 15(11): 7671-7677, 2015.

[25] Papaderakis, A.A. and Dryfe, R.A. The renaissance of electrowetting. *Current Opinion in Electrochemistry.*, 38: 101245, 2023.

[26] Lomax, D.J., Kant, P., Williams, A.T., Patten, H.V., Zou, Y., Juel, A. and Dryfe, R.A. Ultra-low voltage electrowetting using graphite surfaces. *Soft Matter*, 12(42): 8798-8804, 2016.

[27] Papaderakis, A.A., Polus, K., Kant, P., Box, F., Etcheverry, B., Byrne, C., Quinn, M., Walton, A., Juel, A. and Dryfe, R.A. Taming electrowetting using highly concentrated aqueous solutions. *Journal of Physical Chemistry C*, 126(49): 21071-21083, 2022.

[28] Yasuda, S., Tamura, K., Kato, M., Asaoka, H. and Yagi, I., 2021. Electrochemically driven specific alkaline metal cation adsorption on a graphene interface. *Journal of Physical Chemistry C*, 125(40): 22154-22162, 2021.

[29] Papaderakis, A.A., Ejigu, A., Yang, J., Elgendy, A., Radha, B., Keerthi, A., Juel, A. and Dryfe, R.A. Anion intercalation into graphite drives surface wetting. *Journal of American Chemical Society,* 145(14): 8007-8020, 2023.

[30] Zhang, G., Walker, M. and Unwin, P.R. Low-voltage voltametric electrowetting of graphite surfaces by ion intercalation/deintercalation. *Langmuir*, 32(30): 7476-7484, 2016.

[31] An, C., Yuan, Y., Zhang, B., Tang, L., Xiao, B., He, Z., Zheng, J. and Lu, J. Graphene wrapped $FeSe_2$ nano-microspheres with high pseudocapacitive contribution for enhanced Na-ion storage. *Advanced Energy Materials*, 9(18): 1900356, 2019.

[32] Qin, J., Sari, H.M.K., Wang, X., Yang, H., Zhang, J. and Li, X. Controlled design of metal oxide-based (Mn^{2+}/Nb^{5+}) anodes for superior sodium-ion hybrid supercapacitors: Synergistic mechanisms of hybrid ion storage. *Nano Energy*, 71: 104594, 2020.

[33] Li, L., Liu, L., Hu, Z., Lu, Y., Liu, Q., Jin, S., Zhang, Q., Zhao, S. and Chou, S.L. Understanding high-rate K^+-solvent co-intercalation in natural graphite for potassium-ion batteries. *Angewandte Chemie International Edition*, 59(31): 12917-12924, 2020.

[34] Umegaki, I., Kawauchi, S., Sawada, H., Nozaki, H., Higuchi, Y., Miwa, K., Kondo, Y., Månsson, M., Telling, M., Coomer, F.C. and Cottrell, S.P. Li-ion diffusion in Li intercalated graphite C 6 Li and C 12 Li probed by μ^+ SR. *Physical Chemistry Chemical Physics*, 19(29): 19058-19066, 2017.

[35] Wang, D.Y., Wei, C.Y., Lin, M.C., Pan, C.J., Chou, H.L., Chen, H.A., Gong, M., Wu, Y., Yuan, C., Angell, M. and Hsieh, Y.J. Advanced rechargeable aluminium ion battery with a high-quality natural graphite cathode. *Nature Communications*, 8(1): 14283, 2017.

[36] Chen, H., Xu, H., Wang, S., Huang, T., Xi, J., Cai, S., Guo, F., Xu, Z., Gao, W. and Gao, C. Ultrafast all-climate aluminum-graphene battery with quarter-million cycle life. *Science Advances*, 3(12): 7233, 2017.

[37] Cohn, A.P., Muralidharan, N., Carter, R., Share, K., Oakes, L., and Pint, C.L. Durable potassium ion battery electrodes from high-rate co intercalation into graphitic carbons. *Journal of Material Chemistry A*, 4(39): 14954-14959, 2016.

[38] Share, K., Cohn, A.P., Carter, R., Rogers, B. and Pint, C.L. Role of nitrogen-doped graphene for improved high-capacity potassium ion battery anodes. *ACS nano*, 10(10): 9738-9744, 2016.

[39] Balabajew, M., Reinhardt, H., Bock, N., Duchardt, M., Kachel, S., Hampp, N. and Roling, B. In-situ Raman study of the intercalation of bis (trifluoromethyl sulfonyl) imid ions into graphite inside a dual-ion cell. *Electrochimica Acta*, *211*: 679-688, 2016.

[40] Simon, P., Gogotsi, Y. and Dunn, B. Where do batteries end and supercapacitors begin? *Science*, 343(6176): 1210-1211, 2014.

[41] Gogotsi, Y. and Penner, R.M. Energy storage in nanomaterials–capacitive, pseudocapacitive, or battery-like? *ACS nano*, 12(3): 2081-2083, 2018.

[42] Padhi, A.K., Nanjundaswamy, K.S., and Goodenough, J.B. Phospho-olivines as positive-electrode materials for rechargeable lithium batteries. *Journal of Eelectrochemical Society*, 144(4): 1188, 1997.

[43] Manthiram, A., Materials challenges and opportunities of lithium-ion batteries. *Journal of Physical Chemistry Letters*, *2*(3): 176-184, 2011.

[44] Manthiram, A., A reflection on lithium-ion battery cathode chemistry. *Nature Communications*, *11*(1): 1550, 2020.

[45] Armstrong, A.R. and Bruce, P.G. Synthesis of layered LiMnO2 as an electrode for rechargeable lithium batteries. *Nature*, 381(6582): 499-500, 1996.

[46] Yuan, L.X., Wang, Z.H., Zhang, W.X., Hu, X.L., Chen, J.T., Huang, Y.H. and Goodenough, J.B. Development and challenges of $LiFePO_4$ cathode material for lithium-ion batteries. *Energy Environmental Science*, 4(2): 269-284, 2011.

[47] Winter, M., Besenhard, J.O., Spahr, M.E. and Novak, P. Insertion electrode materials for rechargeable lithium batteries. *Advanced Materials*, *10*(10): 725-763, 1998.